Pergamon

Int. J. Solids Structures Vol. 35, Nos 28–29, pp. 3737–3753, 1998

0020–7683/98 $19.00 + .00

PII: S0020–7683(97)00211–4

EFFECTS OF STRAIN HARDENING AND STRAIN-RATE SENSITIVITY ON THE PENETRATION OF ALUMINUM TARGETS WITH SPHERICAL-NOSED RODS

THOMAS L. WARREN* and MICHAEL J. FORRESTAL
Sandia National Laboratories, Albuquerque, NM 87185-0315, U.S.A.

(*Received* 15 *February* 1997; *in revised form* 21 *July* 1997)

Abstract—We present penetration equations for rigid, spherical-nosed rods that penetrate 6061-T651 aluminum targets. The penetration models use the spherical cavity-expansion approximation and constitutive equations for the target that include strain hardening and strain-rate sensitivity. We obtained closed-form penetration equations for an incompressible target material; however, predictions for a compressible target require the numerical solution of a coupled set of nonlinear ordinary differential equations. Numerical results show the effects of compressibility, strain hardening, and strain-rate sensitivity. We also show that our penetration model requires compressibility, strain hardening, and strain-rate sensitivity to obtain good agreement with previously published depth of penetration data for striking velocities between 300 and 1200 m/s. © 1998 Elsevier Science Ltd. All rights reserved.

INTRODUCTION

Analytical methods for penetration mechanics began with the work of Bishop *et al.* (1945). They developed equations for the quasi-static expansions of cylindrical and spherical cavities and used these equations to estimate forces on conical nose punches pushed slowly into metal targets. Later, Goodier (1965) developed a model to predict the penetration depth of rigid spheres launched into metal targets. That penetration model included target inertial effects, so Goodier (1965) approximated the target response by results from the dynamic, spherically symmetric, cavity-expansion equations for an incompressible target material derived by Hill (1948) and discussed by Hill (1950) and Hopkins (1960). More recently, Forrestal *et al.* (1991) and Forrestal *et al.* (1995) developed spherical cavity-expansion penetration models for spherical-nose, rigid rods that penetrate ductile metal targets.

In our recent studies (Forrestal *et al.* 1991; Forrestal *et al.* 1995), we present analytical models and depth of penetration data for high-strength steel, spherical-nose rod projectiles that penetrate 6061-T651 aluminum targets. We obtained compression stress–strain data to 100% true strain at a strain rate of 10^{-2} s^{-1} and used a rate independent, power-law stress–strain law to describe the post-yield material behavior. In addition, we used the spherical cavity-expansion approximation (Forrestal *et al.*, 1995) that approximates the axisymmetric target response with equations derived from spherically symmetric, cavity-expansion analyses. We compared our analytical model with simulations from axisymmetric Lagrangian (Chen, 1995) and Eulerian (Silling, 1995) wavecodes and showed nearly identical agreement with both wavecodes (Forrestal *et al.*, 1995). When we compared our analytical model and wavecode predictions with depth of penetration data for striking velocities between 300 and 1200 m/s, we obtained excellent agreement when we included a tangential stress on the projectile nose corresponding to an assumed Coulomb type sliding frictional resistance. When we neglected sliding friction, the models overpredicted measured penetration depths and differed by about 20% at a striking velocity of 1200 m/s. As previously discussed (Forrestal *et al.*, 1991), we have no data for sliding frictional resistance at fast sliding velocities and large interface stresses. Thus, the introduction of a sliding

* Author to whom correspondence should be addressed.

frictional resistance was a hypothetical explanation to bring the analytical and wavecode models in agreement with the depth of penetration data.

For this study, we use a constitutive equation for the target that includes strain hardening and strain-rate sensitivity. The present constitutive model for the 6061-T651 target material was motivated by recent high strain-rate, Hopkinson bar data (Mosher, 1996) and pressure-shear data (Yadav *et al.*, 1995). In addition, our present penetration model neglects sliding frictional resistance at the projectile nose–target interface. We neglect sliding frictional resistance based on recent detailed computational models by Camacho and Ortiz (1997). Camacho and Ortiz (1997) performed finite-element simulations corresponding to experiments conducted by Forrestal *et al.* (1990) on the perforation of 5083-H131 aluminum plates with tungsten, conical-nosed projectiles. These simulations use a new adaptive meshing technique and a constitutive material law that includes rate-dependent plasticity, heat conduction, and thermal coupling. Camacho and Ortiz (1997) conclude there is an exceedingly small melted layer in the target next to the projectile that provides a nearly frictionless interface.

In summary, this study presents penetration equations for rigid, spherical-nose rods that penetrate 6061-T651 targets. The target constitutive model includes the effect of strain hardening and strain-rate sensitivity. In the next section, we present the target constitutive model and supporting material data. We then develop spherically symmetric cavity-expansion equations that are employed in our penetration equations. Finally, we present our penetration equations and compare the predictions with previously published depth of penetration data.

CONSTITUTIVE MODEL FOR 6061-T651 ALUMINUM

For this study we seek analytical solutions for spherically symmetric cavity-expansion problems to be used for input into our penetration equations. We present a constitutive equation for 6061-T651 aluminum that is convenient for our analysis and represents stress–strain data for strain rates from 10^{-3}–$10^{5}\ \mathrm{s}^{-1}$. For a state of uniaxial stress, the stress–strain relation is given by

$$\sigma = \begin{cases} E\varepsilon, & \sigma \leqslant Y_{\mathrm{d}} \\ Y\left(\dfrac{E\varepsilon}{Y_{\mathrm{d}}}\right)^{n} + \alpha\left(\dfrac{\dot{\varepsilon}}{\dot{\varepsilon}_0}\right)^{m}, & \sigma > Y_{\mathrm{d}} \end{cases}, \tag{1a,b}$$

where σ is the Cauchy stress (true stress), ε is the logarithmic strain (true strain), $\dot{\varepsilon}$ is the strain rate, E is Young's modulus, Y is the quasi-static yield strength, n is the strain hardening exponent, m is the strain-rate sensitivity exponent, $\dot{\varepsilon}_0$ is a reference strain rate, α is a curve fitting parameter with units of stress, and Y_{d} is the dynamic yield stress given by

$$Y_{\mathrm{d}} = Y + \alpha\left(\frac{\dot{\varepsilon}}{\dot{\varepsilon}_0}\right)^{m}. \tag{1c}$$

The first term in (1b) is similar to the modified Ludwik equation (Chakrabarty, 1987) that describes strain hardening and the second term describes the increase in yield stress due to the strain-rate effects (Yadav *et al.*, 1995).

We obtained constants for the constitutive eqn (1) from compressive stress–strain data for 6061-T6511 aluminum (the only difference between 6061-T651 and 6061-T6511 is the outer surface finish) obtained by Mosher (1996) at nominal strain rates (Ramesh and Narasimhan, 1996) of $10^{-3}\ \mathrm{s}^{-1}$ and $5.4\times10^{3}\ \mathrm{s}^{-1}$ and pressure-shear data for 6061-T651 aluminum obtained by Yadav *et al.* (1995) at a nominal strain rate of $10^{5}\ \mathrm{s}^{-1}$. From curve fits to these data, the model parameters are taken as $E = 68.9$ GPa, $Y = 276$ MPa, $n = 0.072$, $\alpha = 32.0$ MPa, $\dot{\varepsilon}_0 = 1000\ \mathrm{s}^{-1}$, and $m = 0.348$. Furthermore, the density of the undeformated target material is $\rho_0 = 2710\ \mathrm{kg/m}^3$, and when compressibility is considered Poisson's ratio

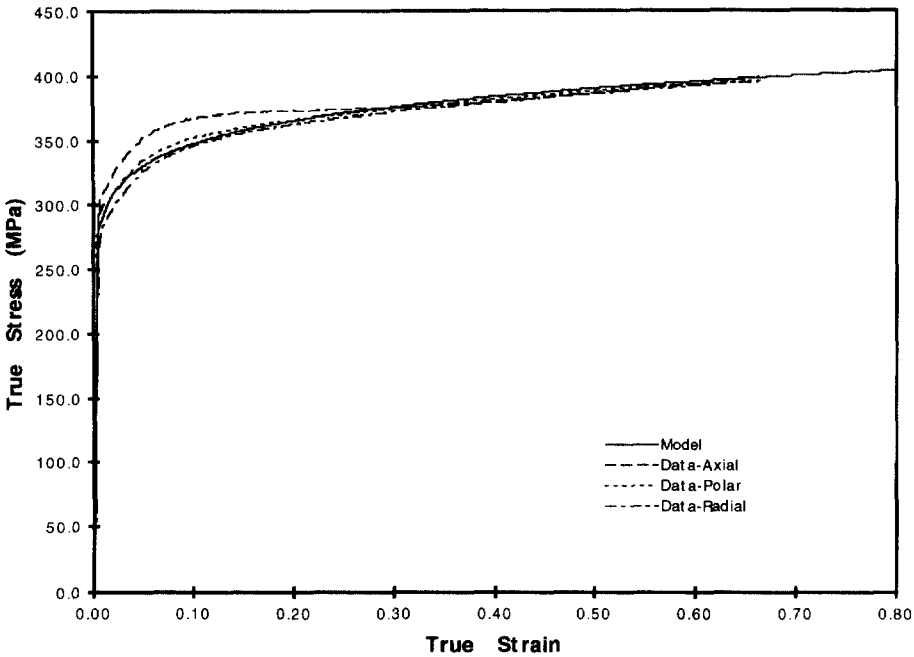

Fig. 1. Stress–strain data and data-fit for the 6061-T6511 aluminum at a nominal strain rate of $\dot{\varepsilon} = 0.001\ s^{-1}$.

is taken as $\nu = 1/3$. Figure 1 shows data and results from (1) for a nominal strain rate of $10^{-3}\ s^{-1}$. For the data in Fig. 1, Mosher (1996) conducted compression experiments at a nominal strain-rate of $10^{-3}\ s^{-1}$ on specimens machined from 254-mm-diameter round stock in the axial, polar and radial directions. Figure 1 shows that for strains less than $\varepsilon = 0.3$ there are some differences in flow stress values for the three orientations which is attributed to the manufacturing process of the round stock. However, for larger strains the behavior in all three directions is nearly identical. Figure 2 shows Hopkinson bar data from an axial specimen (Mosher, 1996) and results from (1) for a nominal strain rate of $5.4 \times 10^3\ s^{-1}$. In both Figs 1 and 2 good agreement is observed between the experimental data and results from the constitutive equation (1). In addition, Yadav *et al.* (1995) report a flow stress of 485 MPa at a strain of $\varepsilon = 0.06$ from a pressure-shear experiment at a nominal strain-rate of $10^5\ s^{-1}$ which is in close agreement with (1) for the selected constitutive model parameters.

In summary, we present a constitutive equation (1) for 6061-T651 aluminum and choose parameters to fit stress–strain data for nominal strain-rates from 10^{-3}–$10^5\ s^{-1}$. From our penetration model we predict peak strain rates of $6.8 \times 10^5\ s^{-1}$ for a projectile striking velocity of 1200 m/s. Klopp *et al.* (1985) present pressure-shear data that suggests that the flow stress does not saturate until the nominal strain-rate is between 10^6 and $10^7\ s^{-1}$, so we assume that (1) is a reasonable approximation for the penetration model presented in this study for projectile striking velocities up to 1200 m/s.

SPHERICALLY SYMMETRIC CAVITY-EXPANSION MODELS

Incompressible, strain hardening, rate-dependent model

In this section the cavity-expansion model described by Hopkins (1960) for an incompressible elastic-perfectly plastic material is extended to include strain hardening and strain-rate dependence through the phenomenological constitutive relation given in (1). For this problem a spherically symmetric cavity is expanded from zero initial radius to radius a. As shown in Fig. 3, this expansion produces plastic and elastic response regions. The plastic region is bounded by the radii $r = a$ and $r = b$, where r is the radial Eulerian coordinate and b is the interface position between the plastic and elastic response regions. Next, we present the equations that govern this problem. Then, we derive our solution.

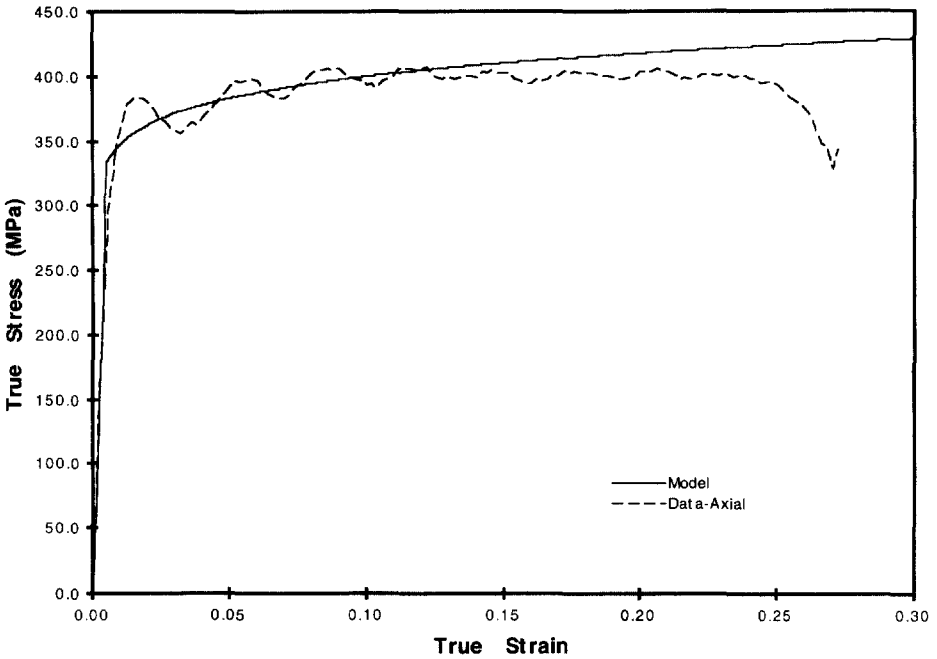

Fig. 2. Stress–strain data and data-fit for the 6061-T6511 aluminum at a nominal strain rate of $\dot{\varepsilon} = 5400\ s^{-1}$.

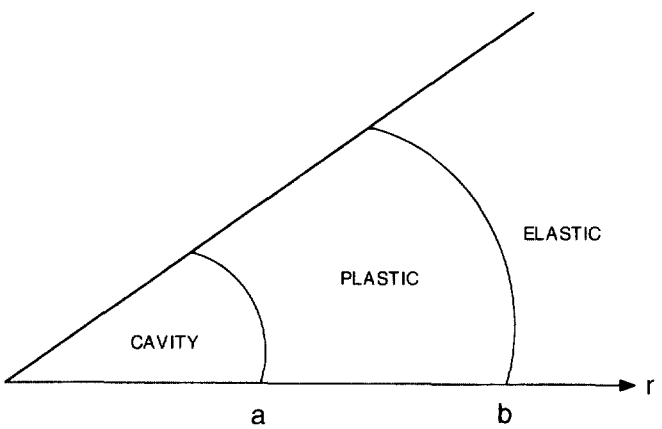

Fig. 3. Response regions for the cavity-expansion problem.

The equations of momentum and mass conservation in Eulerian coordinates with spherical symmetry are

$$\frac{\partial \sigma_r}{\partial r} + \frac{2(\sigma_r - \sigma_\theta)}{r} = -\rho\left(\frac{\partial v}{\partial t} + v\frac{\partial v}{\partial r}\right) \tag{2a}$$

$$\rho_0 \frac{\partial}{\partial r}[(r-u)^3] = 3\rho r^2, \tag{2b}$$

where σ_r, σ_θ are the radial and hoop components of the Cauchy stress, measured positive in compression, and ρ_0 and ρ are the densities in the undeformed and deformed states and are equal when the material is assumed incompressible. Particle displacement u and particle velocity v in the radial direction (outward motion taken positive) are related by

$$\frac{\partial u}{\partial t} = v\left(1 - \frac{\partial u}{\partial r}\right). \tag{3}$$

True strain rates and the logarithmic (true) strain–displacement relations are, respectively,

$$\dot{\varepsilon}_r = -\frac{\partial v}{\partial r}, \quad \dot{\varepsilon}_\theta = -\frac{v}{r}, \tag{4}$$

and

$$\varepsilon_r = \ln\left(1 - \frac{\partial v}{\partial r}\right), \quad \varepsilon_\theta = \ln\left(1 - \frac{u}{r}\right), \tag{5}$$

where $(\dot{.}) \equiv \mathrm{d}(\ldots)/\mathrm{d}t$ (i.e. material derivative operator), and for an incompressible material $\varepsilon_r = -2\varepsilon_\theta$. Equations (2)–(5) along with the constitutive eqn (1) govern this spherically symmetric, incompressible cavity-expansion problem.

Plastic flow is introduced by the method presented by Hill (1950) for the quasi-static spherical cavity-expansion problem and later used by Luk *et al.* (1991) for the dynamic case. This method allows for data obtained from uniaxial compression tests to be directly applied to the cavity-expansion problem. From Hill (1950), the uniaxial stress in (1) is replaced with $(\sigma_r - \sigma_\theta)$ and the uniaxial strain is replaced with ε_r. Thus,

$$\sigma_r - \sigma_\theta = Y\left(\frac{E\varepsilon_r}{Y_d}\right)^n + \alpha\left(\frac{\dot{\varepsilon}_r}{\dot{\varepsilon}_0}\right)^m, \tag{6a}$$

$$Y_d = Y + \alpha\left(\frac{\dot{\varepsilon}_r}{\dot{\varepsilon}_0}\right)^m. \tag{6b}$$

The boundary condition at the cavity surface $r = a$ is

$$u = a(t). \tag{7}$$

Integrating (2b) subject to condition (7) gives the radial particle displacement as

$$u = r\left[1 - \left(1 - \frac{a^3}{r^3}\right)^{1/3}\right]. \tag{8}$$

Particle velocity in the radial direction is obtained by differentiating (8) and substituting into (3) giving

$$v = \frac{a^2\dot{a}}{r^2}, \tag{9}$$

where the cavity radius a is only a function of time. From (4) and (9) the strain rates are

$$\dot{\varepsilon}_r = \frac{2a^2\dot{a}}{r^3}, \quad \dot{\varepsilon}_\theta = -\frac{a^2\dot{a}}{r^3}. \tag{10}$$

Substituting (5), (8), (6b) and (10) into (6a) allows the yield criterion to be expressed in terms of the radial distance r and cavity radius a. Thus,

$$\sigma_r - \sigma_\theta = Y\left(\frac{2E}{3Y}\right)^n \left[\frac{-\ln(1-(a/r)^3)}{1+\psi\dot{a}^m(a/r)^{3m}}\right]^n + \alpha\left(\frac{2a^2\dot{a}}{r^3\dot{\varepsilon}_0}\right)^m, \tag{11a}$$

where

$$\psi = \frac{\alpha}{Y}\left(\frac{2}{a\dot{\varepsilon}_0}\right)^m. \tag{11b}$$

Conservation of momentum (2a) in the plastic region $a \leqslant r \leqslant b$ can be expressed in terms of r and a using (9) and (11). Thus,

$$\frac{\partial\sigma_r}{\partial r} = -\frac{2Y}{r}\left(\frac{2E}{3Y}\right)^n \left[\frac{-\ln(1-(a/r)^3)}{1+\psi\dot{a}^m(a/r)^{3m}}\right]^n - \frac{2\alpha}{r^{3m+1}}\left(\frac{2a^2\dot{a}}{\dot{\varepsilon}_0}\right)^m - \rho_0\left(\frac{\ddot{a}a^2+2a\dot{a}^2}{r^2} - \frac{2a^4\dot{a}^2}{r^5}\right), \tag{12}$$

where (12) can be directly integrated with respect to r throughout the plastic region to obtain σ_r.

In the elastic region $b \leqslant r \leqslant \infty$ displacements and strains are assumed small. Response equations for the elastic region are presented by Hopkins (1960). The particle displacement and particle velocity in the radial direction are

$$u = \frac{a^3}{3r^2}, \quad v = \frac{a^2\dot{a}}{r^2}. \tag{13}$$

The elastic strains are

$$\varepsilon_r = -\frac{\partial u}{\partial r} = \frac{2a^3}{3r^3}, \quad \varepsilon_\theta = -\frac{u}{r} = -\frac{a^3}{3r^3}, \tag{14}$$

and Hook's law for an incompressible material provides the relation

$$\sigma_r - \sigma_\theta = \frac{2Ea^3}{3r^3}. \tag{15}$$

Using (15) with (2a) and integrating gives the radial stress in the elastic region as

$$\sigma_r = \frac{4E}{9}\left(\frac{a}{r}\right)^3 + \frac{\rho_0}{r}(\ddot{a}a^2+2a\dot{a}^2) - \frac{\rho_0\dot{a}^2}{2}\left(\frac{a}{r}\right)^4. \tag{16}$$

For an incompressible material, the Hugoniot interface conditions require that the displacement, velocity, and traction normal to the elastic–plastic interface be continuous (Hopkins, 1960). Thus, integrating (12) between a and b, and using (16) provides the expression for the radial stress at the cavity surface as

$$\sigma_r(a) = \frac{4E}{9}\left(\frac{a}{b}\right)^3 + \frac{2Y}{3}\left(\frac{2E}{3Y}\right)^n \int_0^{1-\left(\frac{a}{b}\right)^3} \frac{[-\ln x]^n}{(1-x)[1+\psi\dot{a}^m(1-x)^m]^n}\,dx + \rho_0\left[\ddot{a}a + \frac{3}{2}\dot{a}^2\right] + \frac{2\alpha}{3m}\left(\frac{2\dot{a}}{a\dot{\varepsilon}_0}\right)^m\left[1-\left(\frac{a}{b}\right)^{3m}\right]. \tag{17}$$

In (17), b is an unknown quantity which is obtained by equating (9) and (15) at the elastic–plastic interface ($r = b$) and solving the nonlinear equation

$$Y - \frac{2Ea^3}{3b^3} + \alpha\left(\frac{2a^2\dot{a}}{b^3\dot{\varepsilon}_0}\right)^m = 0 \tag{18a}$$

using the bisection method as described by Press *et al.* (1989). A close approximation for b can be obtained by an iterative solution of (18a) that recognizes that the last term in (18a) is small. Thus,

$$\left(\frac{a}{b}\right)^3 \approx \frac{3Y}{2E} + \frac{3\alpha}{2E}\left(\frac{3Y\dot{a}}{Ea\dot{\varepsilon}_0}\right)^m. \tag{18b}$$

which can also be used as an initial guess with the bisection method. Once b is obtained, the dynamic flow stress Y_d at the elastic plastic interface is defined by

$$Y_d = \frac{2E}{3}\left(\frac{a}{b}\right)^3. \tag{19}$$

Using (19) in (17) gives the radial stress at the cavity surface which can be written in dimensionless form as

$$\frac{\sigma_r(a)}{Y} = \frac{2}{3}\left[\frac{Y_d}{Y} + \left(\frac{2E}{3Y}\right)^n \int_0^{1-\frac{3Y_d}{2E}} \frac{[-\ln x]^n}{(1-x)[1+\psi\dot{a}^m(1-x)^m]^n}\,dx\right] + \frac{\rho_0}{Y}\left[\ddot{a}a + \frac{3}{2}\dot{a}^2\right] + \frac{2\alpha}{3Ym}\left(\frac{2\dot{a}}{a\dot{\varepsilon}_0}\right)^m\left[1 - \left(\frac{3Y_d}{2E}\right)^m\right]. \tag{20}$$

The first term in (20) corresponds to the strain hardening component of the solution, and in general the integral requires numerical integration using an open integration formula (Press *et al.*, 1989). The second term in (20) corresponds to the inertial part of the solution, and the last term accounts for the strain-rate effects. The last component in the strain-rate term of (20) is generally quite small (i.e. $E \gg Y_d$) and can be neglected. A further simplification of (20) occurs if it is assumed that: (a) $Y_d = Y$ at the elastic plastic interface, and (b) the dynamic effects in the integral in the first term can be neglected. It is found that for the problems of interest these assumptions have only a minor effect on the solution as will be shown later. Thus, with the above simplifications (20) reduces to

$$\frac{\sigma_r(a)}{Y} = \frac{2}{3}\left[1 + \left(\frac{2E}{3Y}\right)^n \int_0^{1-\frac{3Y}{2E}} \frac{[-\ln x]^n}{1-x}\,dx\right] + \frac{\rho_0}{Y}\left[\ddot{a}a + \frac{3}{2}\dot{a}^2\right] + \frac{2\alpha}{3Ym}\left(\frac{2\dot{a}}{a\dot{\varepsilon}_0}\right)^m, \tag{21}$$

where now the rate dependence is confined entirely to the last term in (21). It has also been shown by Forrestal *et al.* (1995) that for long rod projectiles the acceleration component $\ddot{a}a$ has a negligible effect in the equation for the depth of penetration and can also be neglected. In addition (20) and (21) show that the strain-rate term is dependent on the cavity radius; therefore, a similarity solution as used by Forrestal *et al.* (1991) is not possible when strain-rate effects are considered.

Augmented compressible, strain-hardening, rate-dependent model

As shown by (21) and previously discussed, the approximate incompressible solution consists of three uncoupled effects: (a) a quasi-static, strain hardening term, (b) inertial terms, and (c) a strain-rate term. The strain-rate term introduces a length scale which is the cavity radius; therefore, incompressible or compressible cavity-expansion solutions using a similarity transformation are not possible (Luk *et al.*, 1991). We show later in our

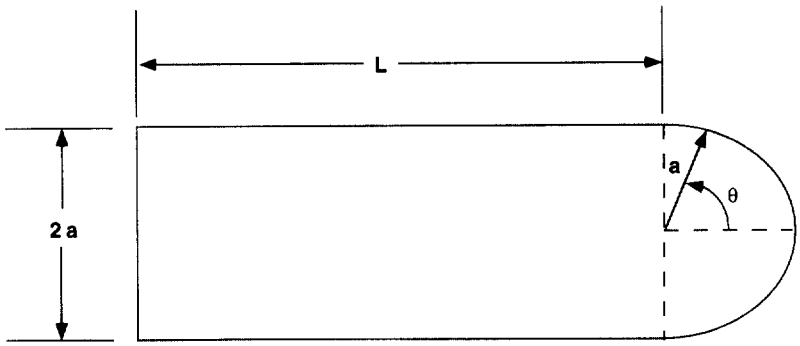

Fig. 4. Projectile geometry.

numerical results that the strain-rate effect is important for high velocity penetration problems, but that the quasi-static, strain hardening and inertial effects dominate the penetration process. Thus, we augment the compressible solution of Luk *et al.* (1991) by adding the strain-rate term derived from the incompressible analysis. We consider the augmented solution to be a reasonable approximation for a strain-rate sensitive, compressible material and later justify this approximation by showing good agreement with penetration depth versus striking velocity data.

The augmented dimensionless radial stress at the cavity surface is given by

$$\frac{\sigma_r(a)}{K} = S_a + \frac{2\alpha}{3mK}\left(\frac{2\dot{a}}{a\dot{\varepsilon}_0}\right)^m \left[1 - \left(\frac{3Y_d}{2E}\right)^m\right], \tag{22}$$

where K is the bulk modulus. The first term S_a in (22) corresponds to the compressible strain-hardening solution (Luk *et al.*, 1991) which is scale independent, and the second term accounts for the strain-rate sensitivity which is dependent on the size of the cavity radius. In the course of this study, we found a way to simplify the computational procedure used by Luk *et al.* (1991) for the compressible strain-hardening solution by obtaining closed-form expressions for the boundary conditions at the elastic–plastic interface. This new procedure to obtain S_a is outlined in the Appendix.

Cavity-expansion numerical results

For input to our penetration models (Forrestal *et al.*, 1995), we require the cavity to be expanded from zero initial radius at a constant cavity-expansion velocity $\dot{a} = V$; therefore, we always consider the cavity-expansion velocity to be constant. Material parameters for the numerical examples are given in the section on the constitutive model. In addition, the cavity radius is taken as $a = 3.55$ mm which corresponds to the radius of the spherical-nosed projectiles used in the penetration experiments as illustrated in Fig. 4. Figure 5 compares results from the incompressible solutions given by (20) and (21) and shows that (21) is an excellent approximation. As previously discussed, (21) consists of a quasi-static strain hardening term, inertial terms, and a strain-rate term. The strain-rate term from (21) is also used in the augmented compressible solution.

Results for the incompressible and compressible models with and without strain rate effects are shown in Fig. 6. It is observed that for all values of dimensionless cavity-expansion velocity the incompressible solution with strain-rate effects produces the largest values of radial stress at the cavity surface. Conversely, the compressible solution without strain rate effects produces the smallest values of radial stress. However, the compressible solution with strain rate effects (i.e. augmented compressible solution) is greater than the incompressible solution without strain rate effects up to about a dimensionless cavity-expansion velocity of two at which point the latter becomes greater.

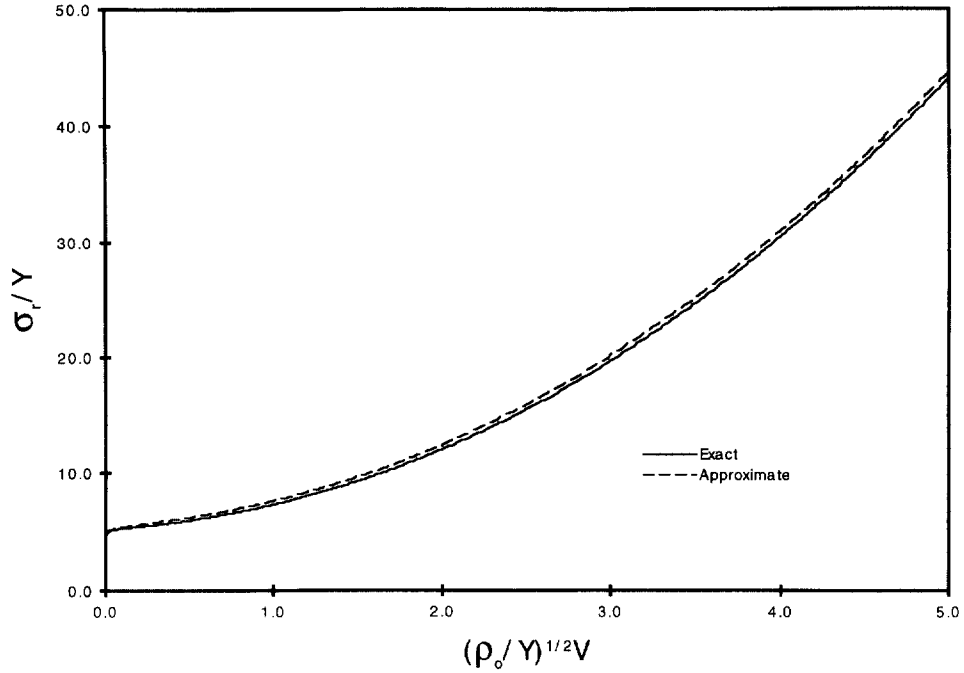

Fig. 5. Radial stress at the cavity surface vs cavity-expansion velocity obtained from the incompressible solutions given by eqns (20) and (21).

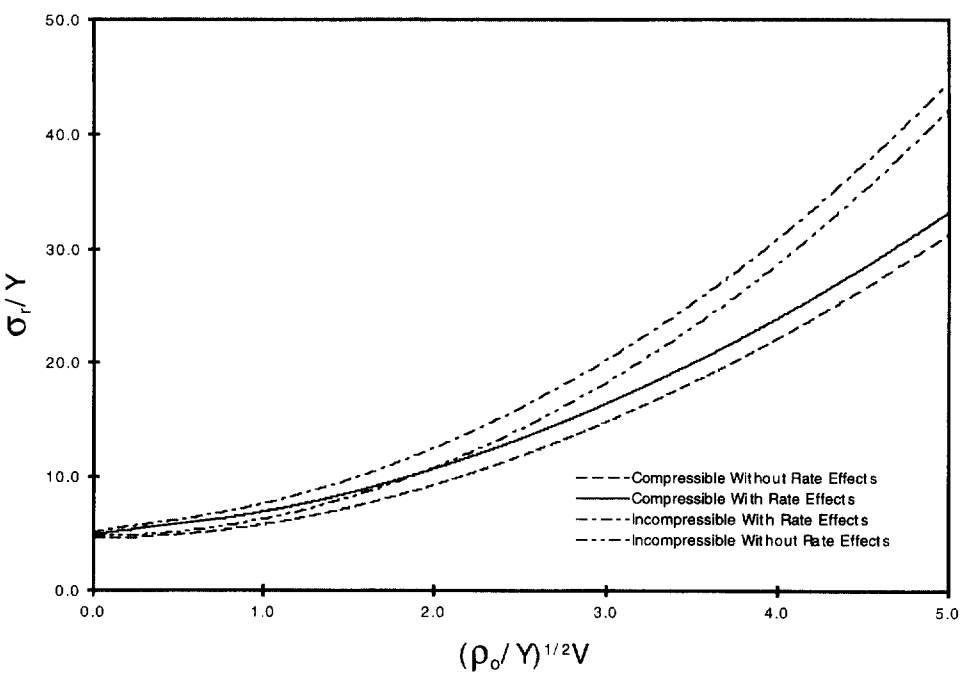

Fig. 6. Radial stress at the cavity surface vs cavity-expansion velocity for the compressible and incompressible models with and without strain rate effects.

PENETRATION MODELS AND COMPARISON OF PREDICTIONS WITH DATA

Penetration equations

In this section we develop penetration equations for rigid spherical-nose rods that penetrate ductile metal targets. The mass of the spherical-nose rod is given by

$$M = \pi a^2 \rho_p \left(L + \frac{2a}{3} \right), \tag{23}$$

where ρ_p is the projectile density, and L and a are the shank length and radius as illustrated in Fig. 4. As shown by Forrestal *et al.* (1988), the axial force acting on the spherical-nose of the projectile is

$$F_z = \pi a^2 \int_0^{\pi/2} \sigma_n(V_z, \theta) \sin(2\theta)\, \mathrm{d}\theta, \tag{24}$$

where $\sigma_n(V_z, \theta)$ is the stress normal to the spherical nose and θ is defined in Fig. 4. In (24), sliding frictional stresses tangent to the spherical-nose have been neglected based on both experimental and numerical results (Camacho and Ortiz, 1997).

From the geometry in Fig. 4, the target particle velocity at the nose–target interface caused by the projectile penetrating at rigid-body velocity V_z is

$$\mathcal{V}(V_z, \theta) = V_z \cos\theta. \tag{25}$$

The normal stress distribution σ_n on the spherical-nose is approximated (Forrestal *et al.*, 1995) by replacing the spherically symmetric cavity-expansion velocity $\dot{a}$ in (21) with (25). Using this result in (24) and integrating gives the axial force acting on the projectile nose due to target resistance as

$$F_z = \pi a^2 Y \left[\Lambda + \frac{2}{3} \rho_0 a \frac{\mathrm{d}V_z}{\mathrm{d}t} + \Psi V_z^2 + \Phi \left(\frac{2V_z}{a\dot{\varepsilon}_0} \right)^m \right], \tag{26a}$$

where

$$\Lambda = \frac{2}{3} \left[1 + \left(\frac{2E}{3Y} \right)^n \int_0^{1 - \frac{3Y}{2E}} \frac{[-\ln x]^n}{1-x}\, \mathrm{d}x \right] \tag{26b}$$

$$\Psi = \frac{3\rho_0}{4Y} \tag{26c}$$

$$\Phi = \frac{4\alpha}{3Ym(2+m)}. \tag{26d}$$

By applying Newton's second law in the axial direction of the projectile and collecting terms we obtain

$$\rho_p \left(L + \frac{2a}{3} \right) \left[1 + \left(\frac{\rho_0}{\rho_p} \right) \frac{1}{(1 + 3L/2a)} \right] \frac{\mathrm{d}V_z}{\mathrm{d}t} = -Y \left[\Lambda + \Psi V_z^2 + \Phi \left(\frac{2V_z}{a\dot{\varepsilon}_0} \right)^m \right]. \tag{27}$$

As shown by Forrestal *et al.* (1995) for steel projectiles ($\rho_p = 8000$ kg/m^3) and aluminum targets ($\rho_0 = 2710$ kg/m^3) with $L/2a = 10$, the second term in the bracket on the left side of (27) gives 0.011 and can be neglected. Integrating (27) to find the final depth of penetration P for a given striking velocity V_s gives

$$\frac{P}{(L + 2a/3)} = \frac{4\Theta}{3} \left(\frac{\rho_p}{\rho_0} \right) \int_0^{\eta} \frac{\zeta\, \mathrm{d}\zeta}{\Lambda + \Theta\zeta^2 + \Phi\zeta^m}, \tag{28a}$$

Table 1. Least-square fit coefficients for the different radial stress models

Model	A	B	C
Incompressible without strain rate effects	4.8376	0.0	1.5
Incompressible with strain rate effects	5.5468	0.6255	1.4377
Compressible without strain rate effects	4.4534	0.4680	0.9926
Compressible with strain rate effects	5.0394	0.9830	0.9402

where the integrand is in a dimensionless form and

$$\Theta = \Psi\left(\frac{a\dot{\varepsilon}_0}{2}\right)^2 \tag{28b}$$

$$\eta = \frac{2V_s}{a\dot{\varepsilon}_0}. \tag{28c}$$

In general m is not an integer and (28a) must be integrated numerically. However, the radial stress at the cavity surface as a function of a cavity-expression velocity can be represented accurately with a least-squares polynomial fit of degree two. Thus,

$$\frac{\sigma_r(a)}{Y} = A + B\left(\sqrt{\frac{\rho_0}{Y}}\vartheta\right) + C\left(\sqrt{\frac{\rho_0}{Y}}\vartheta\right)^2, \tag{29}$$

where A, B, and C are the dimensionless fitting coefficients. Using (29) with (25) in (24) gives the axial force acting on a spherical-nose projectile due to target resistance as

$$F_z = \pi a^2 Y\left[A + \frac{2}{3}B\left(\sqrt{\frac{\rho_0}{Y}}V_z\right) + \frac{1}{2}C\left(\sqrt{\frac{\rho_0}{Y}}V_z\right)^2\right]. \tag{30}$$

Substituting (30) into (27) and integrating to find the final depth of penetration P for a given striking velocity V_s gives

$$\frac{P}{(L+2a/3)} = \frac{1}{C}\left(\frac{\rho_p}{\rho_0}\right)\left\{\ln\left[1 + \frac{2B}{3A}\left(\sqrt{\frac{\rho_0}{Y}}V_s\right) + \frac{C}{2A}\left(\sqrt{\frac{\rho_0}{Y}}V_s\right)^2\right]\right.$$
$$\left. + \frac{4B}{\sqrt{18AC-4B^2}}\left[\tan^{-1}\left[\frac{2B}{\sqrt{18AC-4B^2}}\right] - \tan^{-1}\left[\frac{3C(\sqrt{\rho_0/Y}V_s)+2B}{\sqrt{18AC-4B^2}}\right]\right]\right\}. \tag{31}$$

For compressible target materials, cavity-expansion results are obtained numerically, so we must curve-fit the numerical results in Fig. 6 with the least-squares polynomial fit and use (31) to obtain the final depth of penetration. Dimensionless values of A, B, and C for the various cavity-expansion models are given in Table 1.

Results and comparison with penetration data

We now present numerical results from our penetration models that justify the use of the least-squares fit and show the relative effect of compressibility and strain-rate sensitivity. We then compare predictions from the model that includes strain hardening, compressibility, and strain-rate effects with penetration data. Forrestal *et al.* (1988) and Forrestal *et al.* (1991) present depth of penetration vs striking velocity data for 6061-T651 aluminum

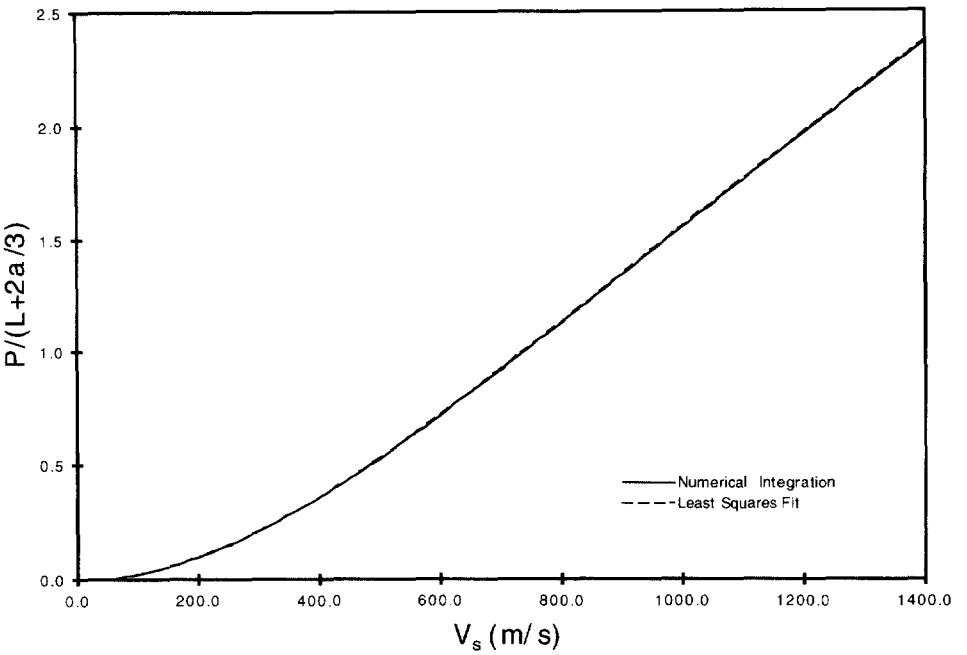

Fig. 7. Scaled depth of penetration vs striking velocity obtained from the incompressible solutions given by eqns (28a) and (31).

targets and maraging steel, spherical-nose rods. For these experiments the rod projectiles had density $\rho_p = 8000$ kg/m^3, shank length $L = 71.12$ mm, nose radius $a = 3.55$ mm, and nominal mass $M = 0.0235$ kg. The aluminum targets were cut from 152 mm diameter 6061-T651 round stock and the material properties are given in the section on the constitutive model.

Results for the dimensionless depth of penetration as a function of striking velocity for an incompressible aluminum target with strain hardening and rate-sensitivity were obtained both by numerically integrating (28a), and also using the closed-form expression in (31) with the representative coefficients from Table 1. The two results are compared in Fig. 7 where it is observed that the difference between the two methods is negligible, which justifies the use of the least-squares fit approximation. Figure 8 shows depth of penetration predictions using (31) for both the incompressible and compressible models with and without strain-rate dependence. In all four cases the least-squares fit approximation was employed and the coefficients for each case are given in Table 1. It is observed in Fig. 8 that the compressible model without strain-rate effects gives the largest depth of penetration which is due to the fact that the model provides the least resistance to penetration. Conversely, the incompressible model with strain-rate effects provides the most resistance to penetration and therefore has the least depth of penetration. In between these two cases lies the results for the compressible model with strain-rate effects and the incompressible model without strain-rate effects. It is observed that at lower velocities the compressible model with strain-rate effects provides more resistance to penetration than the incompressible model without strain-rate effects; however, at approximately 1400 m/s the two models intersect with the latter providing more resistance at striking velocities above 1400 m/s.

In Fig. 9, we compare predictions from the penetration model that includes strain hardening, compressibility, and strain-rate effects with depth of penetration data (Forrestal *et al.*, 1988; Forrestal *et al.*, 1991), and show good agreement. While our predictions in Figs 7–9 extend to $V_s = 1400$ m/s, our data are limited to $V_s = 1200$ m/s. Forrestal *et al.* (1988) attempted penetration experiments at higher striking velocities, but the shank of the maraging steel projectiles always fractured in the penetration tunnel.

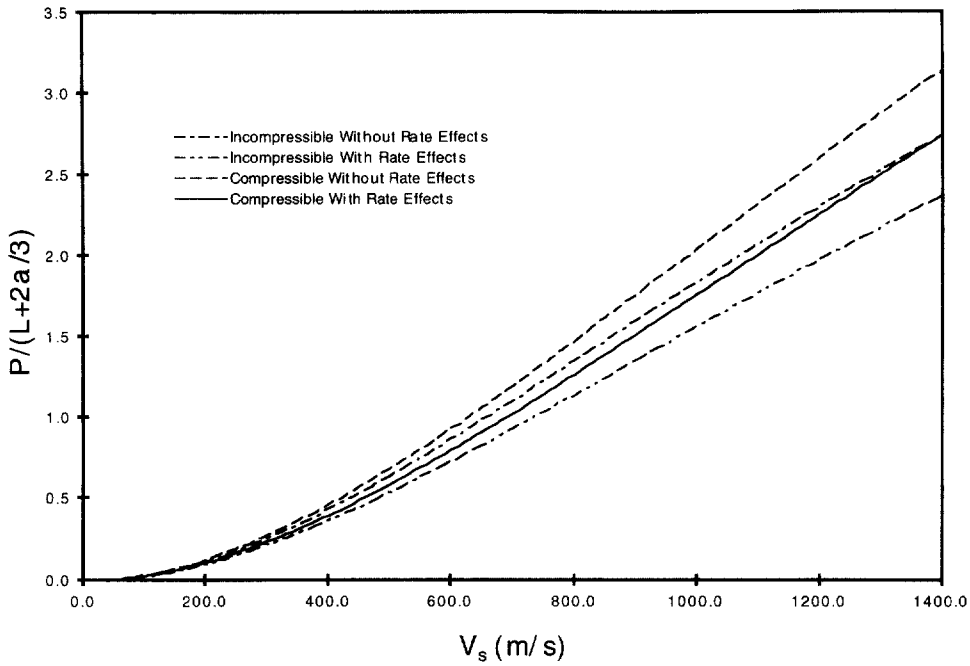

Fig. 8. Scaled depth of penetration vs striking velocity obtained from the compressible and incompressible models with and without strain-rate effects.

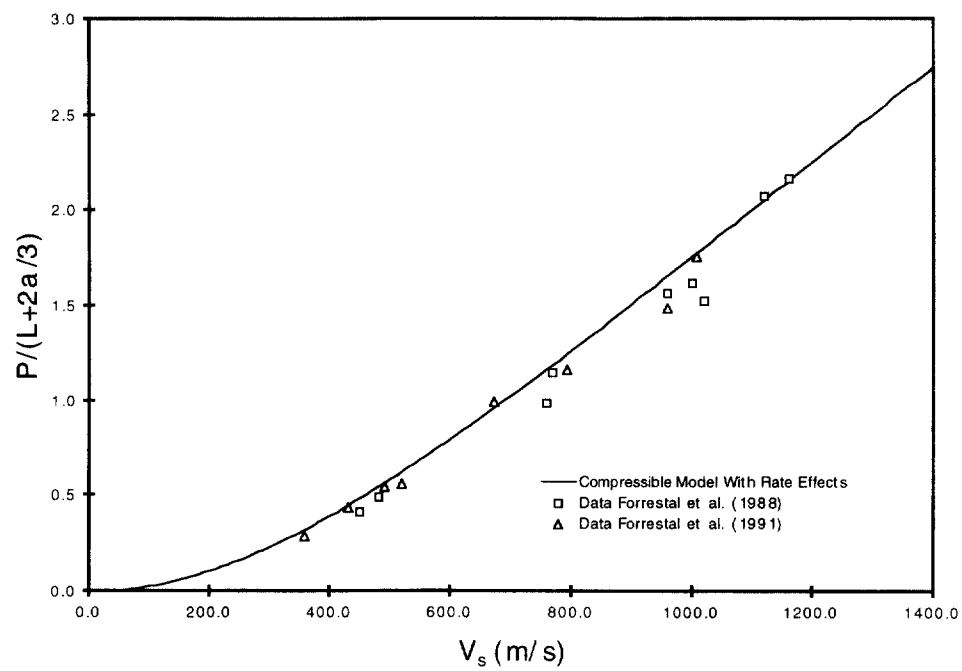

Fig. 9. Scaled depth of penetration vs striking velocity obtained from the compressible model with strain-rate effects and penetration data.

SUMMARY

We present penetration equations for rigid, spherical-nosed rods that penetrate 6061-T651 aluminum targets and show good agreement between predictions and depth of penetration data. Our study starts by presenting a constitutive model and supporting material data for nominal strain-rates between 10^{-3} s^{-1} and 10^{5} s^{-1}. Next, we solve spherically

symmetric, cavity-expansion problems that provide stress distributions for our penetration models. Finally, we develop penetration equations and compare predictions with previously published depth of penetration data for striking velocities to 1200 m/s. Our models show that strain hardening, compressibility, and strain rate effects are all required to obtain good agreement between predictions and data.

Acknowledgements—This work was supported by the United States Department of Energy and the Joint DoD/DOE Munitions Technology Development Program. Sandia is a multiprogram laboratory operated by Sandia Corporation, a Lockheed Martin Company, for the United States Department of Energy under Contract DE-AC04-94AL85000. The authors also gratefully acknowledge numerous discussions with D. E. Amos and D. A. Mosher.

REFERENCES

Bishop, R. F., Hill, R. and Mott, N. F. (1945) The theory of indentation and hardness. *Proceedings of the Royal Society* **57**(3), 147–159.

Camacho, G. T. and Ortiz, M. (1997) Adaptive Lagrangian modeling of ballistic penetration of metallic targets. *Comput. Meth. Appl. Mech. Eng.* **142,** 269–301.

Chakrabarty, J. (1987) *Theory of Plasticity*. McGraw-Hill, New York.

Chen, E. P. (1995) Numerical simulation of penetration of aluminum targets by spherical-nose rods. *Theoretical and Applied Fracture Mechanics* **22,** 159–164.

Forrestal, M. J. and Luk, V. K. (1988) Dynamic spherical cavity-expansion in a compressible elastic–plastic solid. *ASME Journal of Applied Mechanics* **55,** 275–279.

Forrestal, M. J., Brar, N. S. and Luk, V. K. (1991) Penetration of strain-hardening targets with rigid spherical-nose rods. *ASME Journal of Applied Mechanics* **58,** 7–10.

Forrestal, M. J., Luk, V. K. and Brar, N. S. (1990) Penetration of aluminum armor plates with conical-nose projectiles. *Mech. Mater.* **10,** 97–105.

Forrestal, M. J., Okajima, K. and Luk, V. K. (1988) Penetration of 6061-T651 aluminum targets with rigid long rods. *ASME Journal of Applied Mechanics* **55,** 755–760.

Forrestal, M. J., Tzou, D. Y., Askari, E. and Longcope, D. B. (1995) Penetration into ductile metal targets with rigid spherical-nose rods. *International Journal of Impact Engineering* **16**(5/6), 699–710.

Goodier, J. N. (1965) On the mechanics of indentation and cratering in the solid targets of strain-hardening metal by impact of hard and soft spheres. *Proceedings of the 7th Symposium on Hypervelocity Impact III*, pp. 215–259.

Hill, R. (1948) A theory of earth movement near a deep underground explosion. Memo No. 21-48, Armament Research Establishment, Fort Halstead, Kent, U.K.

Hill, R. (1950) *The Mathematical Theory of Plasticity*. Oxford University Press, London.

Hopkins, H. G. (1960) Dynamic expansion of spherical cavities in metals. *Progress in Solid Mechanics Vol.* 1, ed. I. Sneddon and R. Hill. North-Holland, New York, pp. 85–164.

Klopp, R. W., Clifton, R. J. and Shawki, T. G. (1985) Pressure-shear impact and the dynamic viscoplastic response of metals. *Mech. Mater.* **4,** 375–385.

Luk, V. K., Forrestal, M. J. and Amos, D. E. (1991) Dynamic spherical cavity expansion of strain-hardening materials. *ASME Journal of Applied Mechanics*, **58,** 1–6.

Mosher, D. A. (1996) Results from 6061-T6511 aluminum and 4340 steel testing. Private communication, Sandia National Laboratories, Livermore, CA 94551-0969, U.S.A.

Press, W. H., Flannery, B. P., Teukolsky, S. A. and Vetterling, W. T. (1989) *Numerical Recipes, The Art of Scientific Computing*. Cambridge University Press, Cambridge.

Ramesh, K. T. and Narasimhan, S. (1996) Finite deformations and the dynamic measurement of radial strains in compression Kolsky bar experiments. *International Journal of Solids and Structures* **33,** 3723–3738.

Shampine, L. F. and Watts, H. A. (1980) DEPAC-design of a user oriented package of ODE solvers. SAND79-2374, Sandia National Laboratories, Albuquerque, NM.

Silling, S. A. (1994) CTH simulations for spherical-nose steel projectiles into aluminum targets. Private communication, Sandia National Laboratories, Albuquerque, NM 87185-0820, U.S.A.

Yadav, S., Chichilli, D. R. and Ramesh, K. T. (1995) The mechanical response of a 6061-T6 Al/Al_2O_3 metal matrix composite at high rates of deformation. *Acta metall. mater.* **43**(12), 4453–4464.

APPENDIX: COMPRESSIBLE STRAIN-HARDENING CAVITY-EXPANSION MODEL

The description of compressible materials requires the use of the pressure-volumetric strain relation

$$p = \frac{1}{3}(\sigma_r + 2\sigma_\theta) = K(\varepsilon_r + 2\varepsilon_\theta) = K\left(1 - \frac{\rho_0}{\rho}\right), \tag{A1}$$

where K is the bulk modulus which is related to Young's modulus through the relation

$$K = \frac{E}{3(1-2\nu)}. \tag{A2}$$

Due to the fact that Poisson's ratio with compressible materials is not equal to 1/2 requires the plastic flow condition without rate effects to be written as

$$\sigma_r - \sigma_\theta = E^n Y^{1-n}\left[\varepsilon_r - \frac{(1-2\nu)\sigma_\theta}{E}\right]^n. \tag{A3}$$

Following Forrestal *et al.* (1991) by using (A1) and (A2) with the strain definitions (5) in (A3) gives

$$\sigma_r - \sigma_\theta = Y\left(\frac{E}{2Y}\right)^n \left\{\ln\left[\left(1-\frac{\partial u}{\partial r}\right)\left(\frac{r}{r-u}\right)^2\right] + \frac{\sigma_r}{3K}\right\}^n. \tag{A4}$$

Combining (A1) and (A4) to eliminate σ_θ allows the plastic flow rule to be expressed as

$$\sigma_r = \frac{2}{3} Y\left(\frac{E}{2Y}\right)^n \left\{\ln\left[\left(1-\frac{\partial u}{\partial r}\right)\left(\frac{r}{r-u}\right)^2\right] + \frac{\sigma_r}{3K}\right\}^n + K\ln\left[\left(1-\frac{\partial u}{\partial r}\right)\left(1-\frac{u}{r}\right)^2\right]. \tag{A5}$$

Using (5) and (A3) with the similarity transformation

$$\xi = \frac{r}{ct}, \tag{A6a}$$

and dimensionless variables

$$S = \frac{\sigma_r}{K}, \quad \bar{u} = \frac{u}{ct}, \quad T = \frac{Y}{K}, \quad U = \frac{v}{c}, \quad \gamma = \frac{\dot{a}}{c}, \quad \phi = \frac{E}{2Y}, \quad \beta = \frac{c}{c_p}, \tag{A6b}$$

where c is the elastic–plastic interface velocity and $c_p^2 = K/\rho_0$, transforms the momentum and mass conservation equations (2a, b) to

$$\frac{dS}{d\xi} + \frac{2T}{\xi}\phi^n G^n = \left(\frac{\rho}{\rho_0}\right)\beta^2(\xi - U)\frac{dU}{d\xi} \tag{A7a}$$

$$(\xi - \bar{u})^2\left(1 - \frac{d\bar{u}}{d\xi}\right) = \left(\frac{\rho}{\rho_0}\right)\xi^2, \tag{A7b}$$

where

$$G = \ln\left[\left(1-\frac{d\bar{u}}{d\xi}\right)\left(\frac{\xi}{\xi-\bar{u}}\right)^2\right] + \frac{S}{3}. \tag{A7c}$$

Furthermore, using (A6) in (3) gives

$$U\left(1-\frac{d\bar{u}}{d\xi}\right) = \left(\bar{u} - \xi\frac{d\bar{u}}{d\xi}\right). \tag{A8}$$

Combining (A7) and (A8) gives a single equation independent of U and ρ which, when used with (A5), and the transformation

$$\omega = \xi - \bar{u}, \tag{A9}$$

provides two equations for the two unknowns, S and $\bar{u}$. Thus,

$$\frac{dS}{d\xi} + \frac{2T}{\xi}\phi^n G^n = \left(\frac{\beta\omega^2}{\xi\dfrac{d\omega}{d\xi}}\right)^2 \frac{d^2\omega}{d\xi^2} \tag{A10a}$$

$$S = \frac{2T}{3}\phi^n G^n + \ln\left[\frac{d\omega}{d\xi}\left(\frac{\omega}{\xi}\right)^2\right]. \tag{A10b}$$

and

$$G = \ln\left[\left(\frac{\xi}{\omega}\right)^2 \frac{d\omega}{d\xi}\right] + \frac{S}{3}. \tag{A10c}$$

Forrestal and Luk (1988) present solutions for the elastic region from which it follows that on the elastic side of the elastic–plastic interface ($\xi = 1$)

$$\bar{u} = \frac{T(1+\nu)}{9(1-2\nu)}\left[1 - \frac{2\lambda^2}{1+\lambda}\right] \tag{A11a}$$

$$U = \frac{T(1+\nu)}{3(1-2\nu)} \tag{A11b}$$

$$S = \frac{2T}{3}\left[1 + \frac{(1+\nu)\lambda^2}{(1-2\nu)(1+\lambda)}\right], \tag{A11c}$$

where

$$\lambda = \frac{c}{c_d}, \quad c_d^2 = \frac{E(1-\nu)}{(1+\nu)(1-2\nu)\rho_0}, \tag{A12}$$

and c_d is the dilatational wave speed. Hugoniot jump conditions for a spherical cavity expansion in a compressible material require that the displacement, velocity, and traction normal to the elastic–plastic interface be continuous across the interface (Forrestal and Luk, 1988). Thus, the boundary conditions for (A10) at the plastic side of the elastic–plastic interface ($\xi = 1$) are derived using (A9) and (A11) as

$$\omega = 1 - \frac{T(1+\nu)}{9(1-2\nu)}\left[1 - \frac{2\lambda^2}{1+\lambda}\right] \tag{A13a}$$

$$\frac{d\omega}{d\xi} = 1 - \frac{2T(1+\nu)(1-\lambda^3)}{9(1-2\nu)(\lambda^2-1)} \tag{A13b}$$

$$S = \frac{2T}{3}\left[1 + \frac{(1+\nu)\lambda^2}{(1-2\nu)(1+\lambda)}\right]. \tag{A13c}$$

Furthermore, at the cavity surface it is required that

$$\omega(\xi = \gamma) = 0. \tag{A13d}$$

Thus, with the four conditions in (A13), equations (A10) can be solved for the four unknowns ω, $d\omega/d\xi$, S and β.

To obtain the radial stress at the cavity surface in a compressible, strain hardening material, equations (A10) subject to the boundary conditions (A13) are solved numerically using the SLATEC library code DDEABM (Adams–Bashforth–Moulton predictor corrector method) developed by Shampine and Watts (1980). To numerically implement the DDEABM integrator it is required that (A10b) be differentiated and the replacements

$$y_1(\xi) = S(\xi), \quad y_2(\xi) = \omega(\xi), \quad y_3(\xi) = \frac{d\omega(\xi)}{d\xi}, \tag{A14}$$

be made. As shown by Luk *et al.* (1991) using (A14) in (A10) gives the system of three coupled first order nonlinear ordinary differential equations

$$\frac{dy_1}{d\xi} = \frac{H_2 Q_2 - H_3 Q_1}{H_2 - H_1 Q_1} \tag{A15a}$$

$$\frac{dy_2}{d\xi} = y_3 \tag{A15b}$$

$$\frac{dy_3}{d\xi} = \frac{H_3 - H_1 Q_2}{H_2 - H_1 Q_1}, \tag{A15c}$$

where

$$H_1 = 1 - \frac{2}{9} n T \phi^n G^{n-1} \tag{A16a}$$

$$H_2 = -\frac{\left[1 + \frac{2}{3} n T \phi^n G^{n-1}\right]}{y_3} \tag{A16b}$$

$$H_3 = 2\left(\frac{y_3}{y_2} - \frac{1}{\xi}\right)\left[1 - \frac{2}{3}nT\phi^n G^{n-1}\right] \tag{A16c}$$

$$Q_1 = -\left(\frac{\beta y_2^2}{\xi y_3}\right)^2 \tag{A16d}$$

$$Q_2 = -3\left(\frac{2T\phi^n}{3}\right)\frac{G^n}{\xi} \tag{A16e}$$

$$G = \ln\left(\frac{\xi^2 y_3}{y_2^2}\right) + \frac{y_1}{3}. \tag{A16f}$$

With the numerical integration process not only are values of S, ω, and $d\omega/d\xi$ obtained but also the value of γ by using (A13d). Thus, first a value of β [see (A6b)] is selected where $0 \leqslant \beta \leqslant 1$. Integration of (A15) then proceeds through the region $0 \leqslant \gamma \leqslant \xi \leqslant 1$ using the initial conditions (A13a–c) at $\xi = 1$. When $\omega = 0$, γ is known and the expansion velocity and dimensionless radial stress at the cavity surface are obtained from $\dot{a} = \gamma^c$ and $S_a = y_1(\gamma)$, respectively. It must be noted that as $\omega \to 0$, $d\omega/d\xi \to \infty$; however, the DDEABM integrator is robust enough to effectively deal with this adverse situation.